

This is a pre-print version of the paper. Please cite the final version of the paper:

G. Di Martino, A. Di Simone, A. Iodice, G. Poggi, D. Riccio and L. Verdoliva, "Scattering-Based SARBM3D", *IEEE J. Sel. Topics Appl. Earth Observ.*, vol. 9, no. 6, pp. 2131-2144, June 2016. DOI: [10.1109/JSTARS.2016.2543303](https://doi.org/10.1109/JSTARS.2016.2543303).

**IEEE Copyright notice.** © 2016 IEEE. Personal use of this material is permitted. Permission from IEEE must be obtained for all other uses, in any current or future media, including reprinting/republishing this material for advertising or promotional purposes, creating new collective works, for resale or redistribution to servers or lists, or reuse of any copyrighted component of this work in other works.

# Scattering-Based SARBM3D

Gerardo Di Martino, *Member, IEEE*, Alessio Di Simone, Antonio Iodice, *Senior Member, IEEE*, Giovanni Poggi, *Member, IEEE*, Daniele Riccio, *Fellow, IEEE*, and Luisa Verdoliva, *Member, IEEE*

**Abstract**—Interpreting synthetic aperture radar (SAR) images may be a very challenging task, even for expert users. One of the main reasons is the multiplicative speckle noise typical of coherent acquisition systems. Therefore, despeckling can be expected to play a key role in the full exploitation of SAR imagery potential. However, even state-of-the-art despeckling algorithms neglect the physical phenomena hidden behind SAR imagery. Image acquisition depends on electromagnetic scattering, which is also at the basis of speckle noise. Taking into account scattering issues into more physical-based despeckling algorithms may only benefit the overall performance. In this paper, we propose a scattering-based (SB) version of the SAR block-matching 3D (BM3D) filter, named SB-SARBM3D. SARBM3D can be arguably considered as one of the most promising and accurate despeckling algorithms, providing a good compromise between speckle reduction and detail preservation. We modify the original algorithm so as to exploit the prior information available on the imaged scene, taken into account based on scattering concepts. The new algorithm is tested in a variety of different and complementary simulated scenarios, and its performance is assessed objectively by means of numerous synthetic parameters. Moreover, comparison with different state-of-the-art despeckling algorithms is performed on some actual SAR images, both inherent to natural and urbanized areas, for subjective evaluation. Thanks to the prior information, SB-SARBM3D outperforms the original algorithm in terms of both speckle reduction and detail preservation. Moreover, it reduces the annoying artifacts introduced sometimes by SARBM3D in homogeneous areas of the image.

**Index Terms**—Fractals, image denoising, SAR block-matching 3D (SARBM3D), scattering models, synthetic aperture radar (SAR).

## I. INTRODUCTION

**S**YNTHETIC aperture radar (SAR) images are among the most valuable sources of information for all applications involving the remote sensing of the Earth. Besides ensuring all-weather and all-time coverage, they provide information about the surface that cannot be acquired by other types of sensors. However, they are affected by intense speckle, which prevents their use in automatic tools for information extraction, and makes their interpretation challenging even for human experts. Often, this problem is contrasted by resorting to some forms of multilooking, with the remarkable side effect of losing spatial resolution. A more appealing alternative is to resort to signal processing, looking for SAR despeckling techniques that suppress speckle in homogeneous areas without losing resolution

Manuscript received September 30, 2015; revised December 31, 2015; accepted March 10, 2016.

The authors are with the Dipartimento di Ingegneria Elettrica e delle Tecnologie dell'Informazione, Università di Napoli Federico II, 80125 Napoli, Italy (e-mail: gerardo.dimartino@unina.it).

Color versions of one or more of the figures in this paper are available online at <http://ieeexplore.ieee.org>.

Digital Object Identifier 10.1109/JSTARS.2016.2543303

and without impairing the image features of interest. Several techniques have been proposed to tackle this issue [1]. The first approaches known in the literature are local spatial filters [2]–[4], which take into account the nonstationarity of the image by adapting the filter to the local statistics within a fixed-size sliding window. Specifically, most of these filters adopt a test to discriminate homogeneous from heterogeneous areas based on the local coefficient of variation, which is a simple and robust index of textural content. In this way, a good balance between smoothing and edge preservation can be achieved. These techniques have the merit of simplicity but, in general, are characterized by a limited despeckling power. In order to better take into account the characteristics of the scene fluctuations, a Maximum *a Posteriori* (MAP) approach is followed in [5], modeling both the scene and the speckle through a Gamma distribution. Improved versions of these filters have been proposed in [6], using the local coefficient of variation combined with a ratio edge detector [7] not only to inhibit smoothing near edges but also to enhance the edges themselves. In [8], instead, a new model is proposed which better fits SAR data in textured areas, and a more appropriate strategy is used to handle edges and strong scatterers. Still in the context of MAP formulation, a different texture modelization, based on Gauss–Markov Random Fields, is proposed in [9], together with an ad hoc strategy to detect and preserve strong scatterers and borders between regions of uniform backscattering.

More sophisticated methods rely on the use of transforms, which provide a manageable sparse representation of the signal. Several algorithms based on wavelet transform (WT) followed by coefficient shrinkage have been proposed. In particular, by using redundant WT [10], [11], they are also able to avoid annoying artifacts such as Gibbs-like ringing in uniform areas and near edges. In this context, a central issue is the adoption of nonlinear shrinkage for the wavelet coefficients. Even though deterministic shrinkage represents a simple and effective solution, especially in its adaptive version [10], better results can be expected from statistical shrinkage, and its use in the context of MAP approaches has led to a great variety of filters. Also, in this case, results can be improved by taking into account the spatial heterogeneity, as done for example in [12], or in [13], where the local texture energy is used to classify wavelet coefficients and adapt the filtering strategy. More recent techniques which take advantage of bidimensional transforms better fit to represent edges, such as bandelets [14] and curvelets [15]. Instead of using a fixed transform, an alternative approach is to build an adaptive dictionary from the image itself, as done in [16]–[18]. Recently, the nonlocal approach [19] has gained much popularity in this field, proving very effective for various SAR imaging modalities [20]. The basic idea is to take advantage of image

self-similarity. Each target pixel is reconstructed through the weighted average of those pixels that are deemed to be more similar to it. These may be located anywhere in the image, not necessarily close to the target. The central issue, therefore, is to find a suitable measure of similarity, typically patch-based, to find these optimal predictors. Interestingly, a rough form of nonlocal filtering was already present in the well-known sigma filter [21], later improved in [9] and [22]. In recent years, a number of nonlocal techniques have been proposed for SAR despeckling, e.g., [23]–[26]. The most popular among them are arguably PPB [23], characterized by an excellent speckle suppression ability, and SAR-block-matching 3D (SARBM3D) [24], which ensures a very good preservation of fine image features.

All the above-mentioned state-of-the-art techniques are based on statistical and/or geometrical concepts and approaches, with limited physical insight [1], [27]. Even well-known and well-assessed despeckling techniques ([2]–[4]) do not take into any account the physical mechanisms and phenomena involved in SAR image formation. Nonetheless, electromagnetic scattering plays a key role in SAR imagery acquisition process: a SAR image can be modeled as the reflectivity pattern of the illuminated scene filtered by the SAR system [28], [29]. Scattering phenomena are also responsible for the speckle noise that affects every coherent acquisition system like SAR sensors. By explicitly taking into account the electromagnetic phenomena of interest for SAR image formation, notably, the scattering mechanisms, a physical-based approach to despeckling can be pursued. This kind of approach has the potential to provide more reliable and artifact-free SAR images and eventually more informative SAR products, readable also by nonexpert SAR users. A first attempt in this direction, only applicable to polarimetric SAR data, can be found in [30]. More recently, some of the authors applied the aforementioned ideas in a novel physical-based nonlocal means despeckling algorithm in which the measure of object similarity also takes into account the physical parameters [31], [32]. In this paper, we go one step further in this direction, proposing a modified version of the SARBM3D filter [24] where prior information on the scene scattering properties is suitably modeled and taken into account. This paper is organized as follows. Section II provides a detailed description of SARBM3D; proposed modifications to this filter are presented and described in Section III together with the adopted scattering model. In Section IV, the performance improvement over SARBM3D is assessed by computing several objective indicators on some suitable simulated test images. Then, a comparison with state-of-the-art reference techniques is carried out on real-world SAR images. Conclusion is drawn in Section V.

## II. SARBM3D

In this section, we provide the information on SARBM3D strictly necessary for a full understanding of the proposed extension. After a conceptual overview of BM3D, we explore its SAR-oriented version in more detail, introducing also the notation used in the following, and eventually highlight its

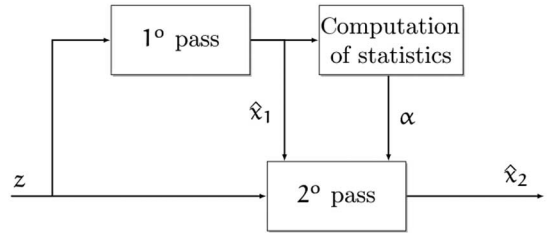


Fig. 1. Block-scheme of the two-pass SARBM3D filter.

strengths and weaknesses. For more information, the reader is referred to the original papers [24], [33].

### A. Block Matching 3-D

As the name suggests, SARBM3D is the SAR-oriented version of the BM3D algorithm, proposed in [33] for AWGN image denoising. While these algorithms share the same general structure, they differ profoundly in the implementation, as SARBM3D takes into account the peculiar nature and strong intensity of speckle noise. The filtering procedure comprises two passes, as shown in Fig. 1.

However, the actual despeckling takes place only in the second pass, by means of Wiener filtering in the wavelet domain. Nonetheless, the first pass is of paramount importance. In fact, it produces a partially despeckled image,  $\hat{x}_1$ , used as a “pilot,” over which the statistics  $\alpha$  for the subsequent Wiener filtering are estimated. The better the pilot, the more reliable the estimates, the better the final outcome. Both in the first and second pass, three main processing steps are carried out:

- 1) grouping;
- 2) collaborative filtering;
- 3) aggregation.

In the grouping step, the nonlocal principle comes heavily into action. For each target block, the most similar blocks in the neighborhood are located and collected in a three-dimensional (3-D) stack for subsequent filtering (see Fig. 2).

By doing so, one exploits the inherent self-similarity of images to mimic a true statistical filtering, where multiple instances of the same block are taken into account. The collaborative filtering of the 3-D stack is performed by wavelet shrinkage, exploiting redundancies both in space and through blocks to separate signal from noise. Finally, the filtered blocks are returned to their original locations and aggregated, gaining the benefit of multiple alternative estimates of the same object.

### B. Dealing With the SAR Despeckling Problem

SARBM3D departs from its AWGN counterpart under two respects: 1) the use of a block similarity measure tailored to speckle statistics; 2) the use of undecimated WT and Wiener filtering in place of ordinary WT and hard thresholding in the first pass. Following the usual multiplicative noise model, the observed signal is expressed as

$$z(s) = x(s)n(s) \quad (1)$$

where the spatial location is indicated by a single letter for compactness,  $z(s)$  and  $x(s)$  are the observed and clean signal

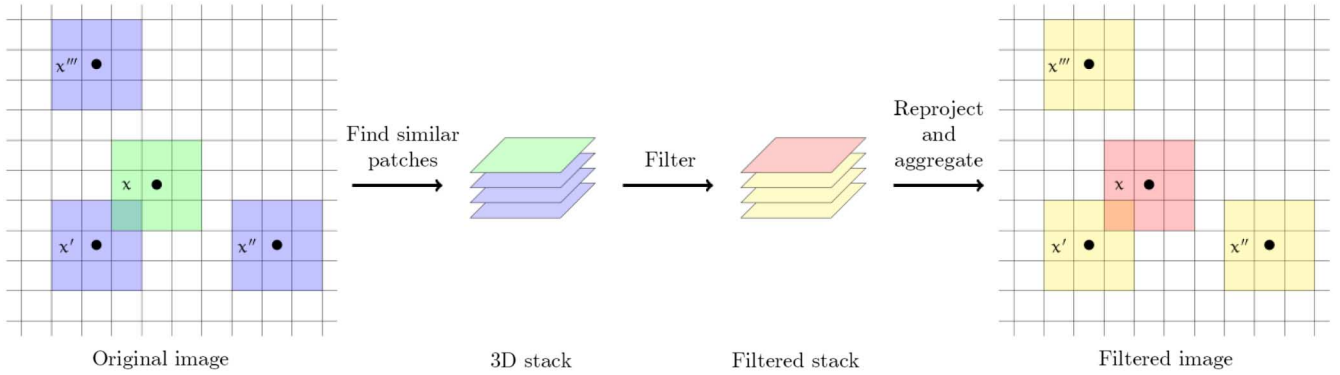


Fig. 2. Nonlocal BM3D in SARBM3D. Inspired to [20, Fig. 2].

intensities, and the speckle samples  $n(s)$  are independent and identically distributed Gamma random variables. Accordingly,  $\hat{x}_1(s)$  and  $\hat{x}_2(s)$  are the intensities estimated in the first and second pass.

Nonlocal filtering relies heavily on a suitable measure of similarity. The problem of determining such a measure, depending on noise statistics, has been studied in several papers [34]–[36]. A widespread approach, well supported by experimental evidence, is to define the similarity between two noisy observations as the likelihood that they come from the same underlying signal before being corrupted by noise, i.e.,

$$p[a(s), a(t) | x(s) = x(t)] \quad (2)$$

where, following [23], we use signal amplitudes  $a(s) = \sqrt{z(s)}$ , rather than intensities, and  $p$  indicates a probability density function. In the hypotheses of additive white Gaussian noise, this approach leads to the Euclidean distance as a measure of dis-similarity. With  $L$ -look SAR images, however, it leads to a different distance

$$d_1[a(B_s), a(B_t)] = (2L - 1) \sum_k \log \left[ \frac{a(s+k)}{a(t+k)} + \frac{a(t+k)}{a(s+k)} \right] \quad (3)$$

where  $B_s$  indicates a block centered on  $s$ ,  $a(B_s)$  is the corresponding amplitude, and  $k$  scans the block pixels. This distance has been used with success in several nonlocal despeckling techniques. Besides having solid statistical bases, using the ratio of samples rather than their difference makes full sense for multiplicative noise, as it makes the distance independent of the average signal level. When other estimates of the signal are available, coming for example from other sensors [37], the distance can be modified to take into account this side information. This is the case of the second pass of SARBM3D, where the first-pass pilot estimate is already available and the distance is therefore modified accordingly.

The other major innovation introduced in SARBM3D concerns the first-pass filtering step aimed at providing the pilot image. As already said, a good pilot is essential for the success of the final despeckling step, especially when the original image is very noisy, as is the case of single-look SAR images. Hence, it makes full sense replacing hard and soft wavelet thresholding with Wiener filtering, which is theoretically optimal. To perform well, however, the latter needs reliable estimates of

statistics. When this is not the case, a simpler but more robust thresholding may still be preferable. To address this issue, SARBM3D resorts to undecimated discrete wavelet transform (UDWT) rather than critically sampled WT. Without decimation, a large number of samples (though more correlated) become available in each subband to estimate the variance of wavelet coefficients, allowing for the correct functioning of the Wiener filter. The price to pay is an increase in computation time and memory usage, more and more acceptable as technology progresses.

In [24], the multiplicative noise model is first of all converted in an additive signal-dependent noise model

$$z(s) = x(s)n(s) = x(s) + x(s)[n(s) - 1] = x(s) + v(s). \quad (4)$$

Then, resorting to some reasonable simplifications, the filtered wavelet coefficients are computed as

$$\hat{X}_1(i) = \max \left( 0, \frac{\langle Z^2 \rangle_{SB(i)} - \frac{\sigma_u^2}{(1+\sigma_u^2)} \langle z^2 \rangle_G}{\langle Z^2 \rangle_{SB(i)}} \right) Z(i) \quad (5)$$

where capital letters indicate wavelet coefficients. In (5), all quantities within the crochets can be estimated reliably by sample averages [24], either over the UDWT subband the coefficient belongs to  $\langle \cdot \rangle_{SB}$  or over the whole 3-D stack  $\langle \cdot \rangle_G$ . Inverse transform provides eventually the filtered image.

### C. Strengths and Weaknesses

We now focus on the pros and cons of SARBM3D, only partially highlighted in the above description. Its major strength is certainly the ability to preserve image details, such as man-made structures, textures, and region boundaries. This is due to the nonlocal approach. Since details represent rare “anomalies” as opposed to the larger homogeneous areas, it is only by collecting multiple similar patches in a large area that one can gather enough information to perform a reliable estimation. This information is then exploited very effectively in SARBM3D by means of a number of sophisticated tools, such as UDWT, Wiener filtering, and the aggregation of multiple estimates. The strengths of SARBM3D, however, are also its weaknesses. Since it preserves very well image structures, it tends to preserve also random patterns originated by speckle

in homogeneous areas. Therefore, the speckle suppression in homogeneous areas is not as strong as it happens with some competing techniques, e.g., PPB. On the other hand, speckle suppression and detail preservation are inherently contrasting requirements. Interestingly, the reinforcement of random patterns gives rise to despeckling artifacts only occasionally. This important property must be credited to the UDWT/Wiener suite in the first pass which produces a pilot image free of the typical wavelet-basis artifacts. In fact, replacing UDWT with WT, as done in FANS [25] to reduce complexity, originates a number of annoying artifacts. It is therefore reasonable to expect that further improving the pilot, by using some available side information, will entail significant benefits on the final filtered image.

### III. SCATTERING-BASED SARBM3D

As described in the previous section, the first step of SARBM3D aims at estimating the local statistics of image intensity, which are used to drive the actual despeckling process performed in the second step. The quality of such estimates impacts heavily on the filter performance in terms of both speckle rejection and detail preservation. In this paper, we improve the estimation quality using some prior information available on the sensed surface, interpreted through suitable scattering models. As a result, filtering performance improves significantly wherever the proposed scattering model is applicable, and notably in natural areas with gentle topography. In the following, the adopted scattering model and the proposed SB-SARBM3D filter are described in detail.

#### A. Scattering Model

The scattering mechanisms involved in SAR image formation are numerous and complex. They depend on the surface geometry and composition, as well as on SAR operating frequency. Surface and volumetric scattering dominate in natural areas, while double- and multiple-bounce scattering phenomena are evident in urban areas. Taking into account all of these mechanisms in a scattering model would require very involved formulas, with plenty of parameters to estimate or nonclosed form solutions. For the sake of simplicity, we will therefore consider only surface scattering, which is suitable for the description of scattering from natural areas.

A closed-form scattering model, necessary for automatic SAR inversion techniques, requires a suitable model of the surface. To this aim, we resort to the fractal geometry, arguably the best tool for taking into account the self-affinity and self-similarity properties of natural surfaces [38]–[41]. With this approach, a natural surface is described by means of a two-dimensional (2-D) fractional Brownian motion (fBm) stochastic process,  $z(x, y)$ , defined by the relation [40]

$$\Pr \{z(x, y) - z(x', y') < \bar{\zeta}\} = \frac{1}{\sqrt{2\pi}T^{(1-H)}\tau^H} \int_{-\infty}^{\bar{\zeta}} \exp\left(-\frac{\zeta^2}{2T^{2(1-H)}\tau^{2H}}\right) d\zeta \quad (6)$$

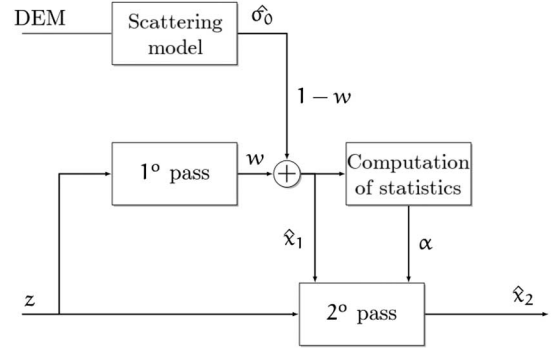


Fig. 3. Block scheme of the SB-SARBM3D algorithm.

where  $\Pr\{\}$  stands for “probability,”  $\bar{\zeta}$  is the considered height increment, and  $z(x, y)$  is the surface elevation

$$\tau = \sqrt{(x - x')^2 + (y - y')^2} \quad (7)$$

is the distance between the two points of coordinates  $(x, y)$  and  $(x', y')$ ,  $H$  is the Hurst coefficient ( $0 < H < 1$ ) related to the fractal dimension  $D = 3 - H$ , and  $T$  is the topography [m], i.e., the distance over which chords joining points on the surface have a root mean square slope equal to unity.

Given the geometrical description of the surface, the scattering model provides its electromagnetic description, i.e., the normalized radar cross section (NRCS). In this paper, we resort to the small perturbation method (SPM) suitable for natural surfaces with limited roughness. Considering a monostatic radar, and assuming that the surface can be described through a fBm, the SPM estimate,  $\hat{\sigma}^0$ , of the NRCS,  $\sigma^0$ , is given by [42], [43]

$$\hat{\sigma}_{mn}^0 = 2\pi 8k^4 S_0 |\beta_{mn}|^2 \frac{\cos^4 \vartheta}{(2k \sin \vartheta)^{2+2H}} \quad (8)$$

in which  $m$  and  $n$  denote the transmitted and received polarizations, either horizontal or vertical,  $k$  is the electromagnetic wavenumber of the incident field, and  $S_0$  is a parameter related to  $T$  and  $H$  [40] characterizing the spectral behavior of the fBm surface. Finally,  $\beta_{mn}$  accounts for the incident- and reflected-field polarization, and is a function of both the complex relative dielectric constant  $\varepsilon_{rc}$  of the surface and the local incidence angle  $\vartheta$  [40]

$$\beta_{hh} = \frac{\cos \vartheta - \sqrt{\varepsilon_{rc} - \sin^2 \vartheta}}{\cos \vartheta + \sqrt{\varepsilon_{rc} - \sin^2 \vartheta}},$$

$$\beta_{vv} = (\varepsilon_{rc} - 1) \frac{\sin^2 \vartheta - \varepsilon_{rc} (1 + \sin^2 \vartheta)}{\varepsilon_{rc} \cos \vartheta + \sqrt{\varepsilon_{rc} - \sin^2 \vartheta}}. \quad (9)$$

Note that, according to this model,  $\beta_{mn} = 0$  for  $m \neq n$ , hence we are able to deal only with the copolarized case. However, a nonnull closed-form expression of the NRCS for the cross-polarized case can be still obtained extending the SPM using the polarimetric two-scale model, described in [44]. From now on, the subscripts related to the polarization will be neglected. Equation (8) describes the NRCS of a single resolution cell with a microscopic roughness described by the fractal parameters  $H$  and  $T$ , and with a macroscopic roughness described by the local incidence angle,  $\vartheta$ , where the latter

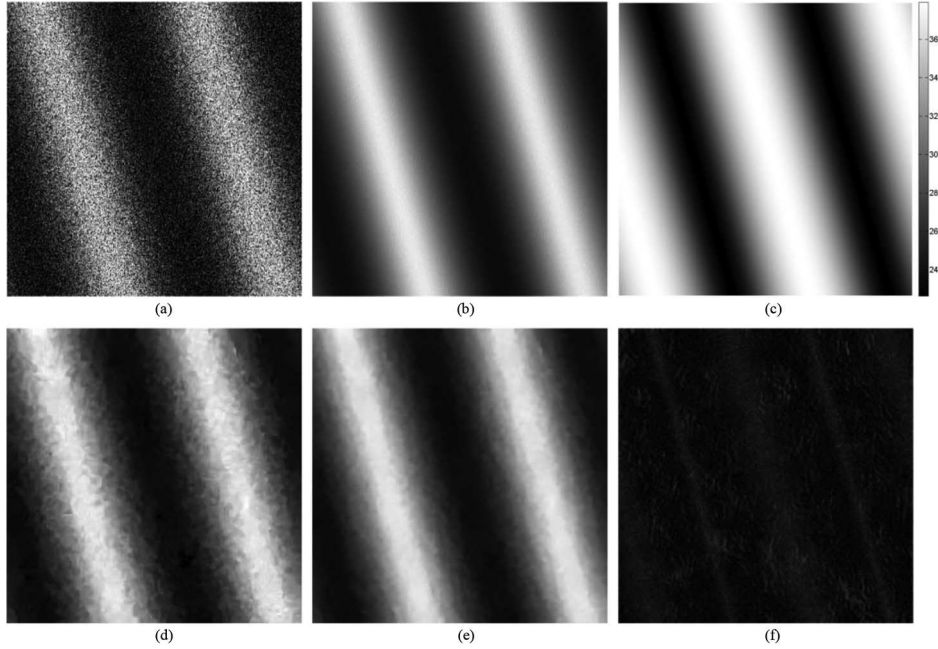


Fig. 4. (a)  $512 \times 512$  simulated single-look SAR image in the presence of a sinusoidal topography, microscopic roughness of fractal parameters  $H = 0.8$  and  $T = 10^{-4}$  m, and electromagnetic parameters  $\epsilon_r = 4$  and  $\sigma_c = 10^{-2}$  S/m. (b) 512-look reference image. (c) Local incidence angle map. (d) SARBM3D. (e) SB-SARBM3D. (f) Weight map in the range 0–1.

is defined as the angle between the propagation direction of the incoming radar electromagnetic wave and the direction orthogonal to the local mean plane approximating the resolution cell. It is noticeable that the proposed surface and scattering models correctly describe single-bounce phenomena occurring on natural surfaces, i.e., multiple-bounce and volume-scattering phenomena—mainly inherent to man-made and vegetated areas—are not taken into account.

The exact evaluation of the surface NRCS via (8) requires the knowledge of a number of surface parameters, such as complex dielectric constant, local incidence angle, microscopic roughness, and topography. Although it is not reasonable to know in advance all these information (which would make useless the SAR image itself), some important parameters can be obtained quite easily. In particular, the local incidence angle can be estimated from a digital elevation model (DEM) of the sensed surface, if available. The estimate reads as

$$\vartheta = \cos^{-1} \left( \frac{p \sin \theta_0 + \cos \theta_0}{\sqrt{p^2 + q^2 + 1}} \right) \quad (10)$$

where  $\theta_0$  is the radar look angle (i.e., the incidence angle over an horizontal surface), and  $p$  and  $q$  are the range and azimuth slopes, respectively, i.e.,  $p = \frac{\partial z}{\partial y}$ ,  $q = \frac{\partial z}{\partial x}$ ,  $z$  being the elevation.

The ability to retrieve the incidence angle is a key ingredient of our proposal. In fact, the SPM NRCS depends heavily on this parameter and much less on other ones, such as relative dielectric constant, electrical conductivity, and topography [32]. Therefore, a good estimate of the NRCS can be obtained even based on this only information. To this end, the local incidence angle map has to be projected into the SAR system geometry and coregistered to the noisy SAR image. The microscopic roughness, instead, can be estimated from the SAR

image via the algorithm developed by Di Martino *et al.* [28] if one assumes that the same value of  $H$  holds at both macroscopic and microscopic scales. This latter is a rather strong assumption, but again, the sensitivity analysis shows that errors on the value of  $H$  do not appreciably affect scattering evaluation if a significant topography is present. In conclusion, the NRCS can be estimated based only on the scene DEM, and the approximation is quite accurate where surface scattering is the dominant scattering component, namely, in natural areas with gentle topography or homogeneous flat regions.

### B. Scattering-Based SARBM3D

The previous section provided insight into how the available information on the scene DEM can be converted, through appropriate scattering models, into an estimate,  $\hat{\sigma}^0$ , of the image NRCS. Our aim is to combine this information with the first-step estimate  $\hat{x}_{1,SARBM3D}$  of SARBM3D to form a better pilot image for the second pass to work on, according to the relation

$$\hat{x}_{1,SB-SARBM3D} = f(\hat{x}_{1,SARBM3D}, \hat{\sigma}^0). \quad (11)$$

The problem becomes, therefore, the design of the most suitable combination function  $f$ .

To this end, it is worth reminding that the available prior information allows for an accurate description of the signal backscattered from natural areas with gentle topography or homogeneous flat regions, where surface scattering is the dominant phenomenon. On the contrary, the description is not reliable in correspondence of nontopographic edges, and in the presence of particular scattering phenomena, such as multiple bounce and volume scattering, typical of vegetated and urban areas. On the other hand, SARBM3D, even in the

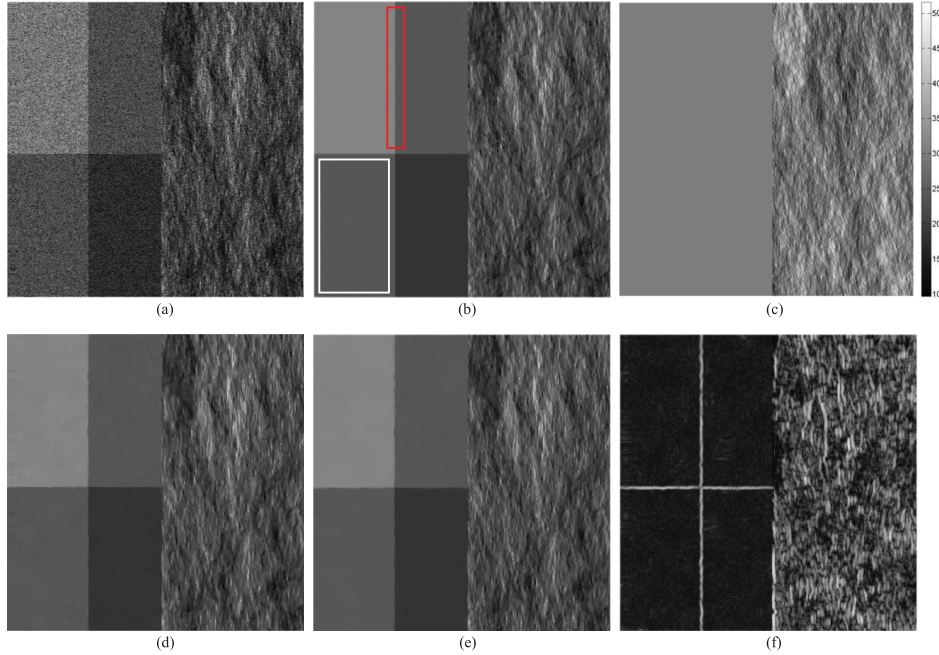


Fig. 5. (a)  $512 \times 512$  simulated single-look SAR image in the presence of a fBm topography of fractal parameters  $H = 0.8$  and  $T = 10^{-4}$  m, and electromagnetic parameters  $\epsilon_r = 4$  and  $\sigma_c = 10^{-2}$  S/m (right) and patches of different electromagnetic parameters—in particular, the brightest square simulates damp soil ( $\epsilon_r = 10$ ,  $\sigma_c = 10^{-2}$  S/m), the middle gray-level squares represent dry soil ( $\epsilon_r = 4$ ,  $\sigma_c = 10^{-3}$  S/m), and the darkest one is sea ( $\epsilon_r = 80$ ,  $\sigma_c = 4$  S/m). (b) 512-look reference image. (c) Local incidence angle map. (d) SARBM3D. (e) SB-SARBM3D. (f) Weight map in the range 0–1. White box indicates the region where the ENL is computed; ES evaluation is performed in the red marked area consisting of 240 horizontal profiles.

TABLE I  
PERFORMANCE PARAMETERS FOR THE SINUSOIDAL DEM

	Moi	VoR	SNR	$C_\kappa$	MSSIM
Clean	1.000	0.997	$\infty$	0.860	1.000
Noisy	1.000	–	–3.693	1.572	0.970
SARBM3D	0.985	0.858	16.045	<b>0.862</b>	0.999
SB-SARBM3D	<b>0.989</b>	<b>0.989</b>	<b>19.296</b>	0.857	<b>1.000</b>

first step, guarantees mostly complementary properties. Edges, man-made regions, and fine details are estimated faithfully, while limited speckle suppression is observed in homogeneous areas, together with some filtering artifacts due to block matching. Based on these observations, we define the function  $f$  so as to perform a simple weighted averaging of the two quantities (normalized to their mean values), with weights  $w(s)$  that adapt pixelwise to the local image content

$$\hat{x}_{1,SB-SARBM3D}(s) = w(s)\hat{x}_{1,SARBM3D}(s) + (1 - w(s))\hat{\sigma}^0(s). \quad (12)$$

Accordingly, the block scheme of Fig. 1 is modified as shown in Fig. 3. As both (12) and the block scheme in Fig. 3 reveal, the proposed modification of SARBM3D is still applicable to both single and multilook SAR data, since the *a priori* scattering information is not affected by the number of looks of the SAR image. Consequently, the SB-SARBM3D filter inherits the applicability of the SARBM3D filter to both single and multilook SAR data.

The weight  $w$  varies in the range 0–1 adaptively across the image, combining in a suitable way the two contributors: large weights give more importance to the first-step SARBM3D

estimate,  $\hat{x}_{1,SARBM3D}$ , while prior knowledge on scattering becomes dominant with small weights. Therefore, for what previously stated, the weight should be close to 1 in correspondence of nontopography-related edges and urban areas (if present), and close to 0 in natural areas with gentle topography or homogeneous flat regions. Therefore, to define a sensible weight map, one has to identify beforehand nontopographic edges and man-made structures. To this aim, we apply to the input SAR image the detectors proposed by Lopes *et al.* [7], [45] which identify relevant image features, such as edges, lines, and point scatterers. To take into account the multiplicative nature of speckle, these detectors operate on local intensity ratios, rather than on the gradients considered in additive-noise contexts. Moreover, to reduce the effects of speckle, ratios are not computed between single-pixel values, but rather between averages taken over suitable windows in the neighborhood of the target pixel (the reader is referred to [7] and [45] for a more detailed description). In this work, we use the very same windows defined in [45] for detecting edges, lines, and strong scatterers. Even so, the output detection map appears to be quite noisy, with many false alarms and missed detections. To improve reliability, we could enlarge the reference windows, but this would entail an unacceptable loss of spatial resolution. Instead, we resort here to the virtual multilooking technique introduced in [46] based itself on nonlocal estimation. For each patch of the SAR image, a number of similar patches are collected over a large neighborhood, using block matching with the distance measure of (3). These are averaged together, with no loss of spatial resolution, to obtain a much cleaner patch to which the detectors of [45] are eventually applied. The output ratio map  $r_I$  takes values in the range 0–1, as explained in

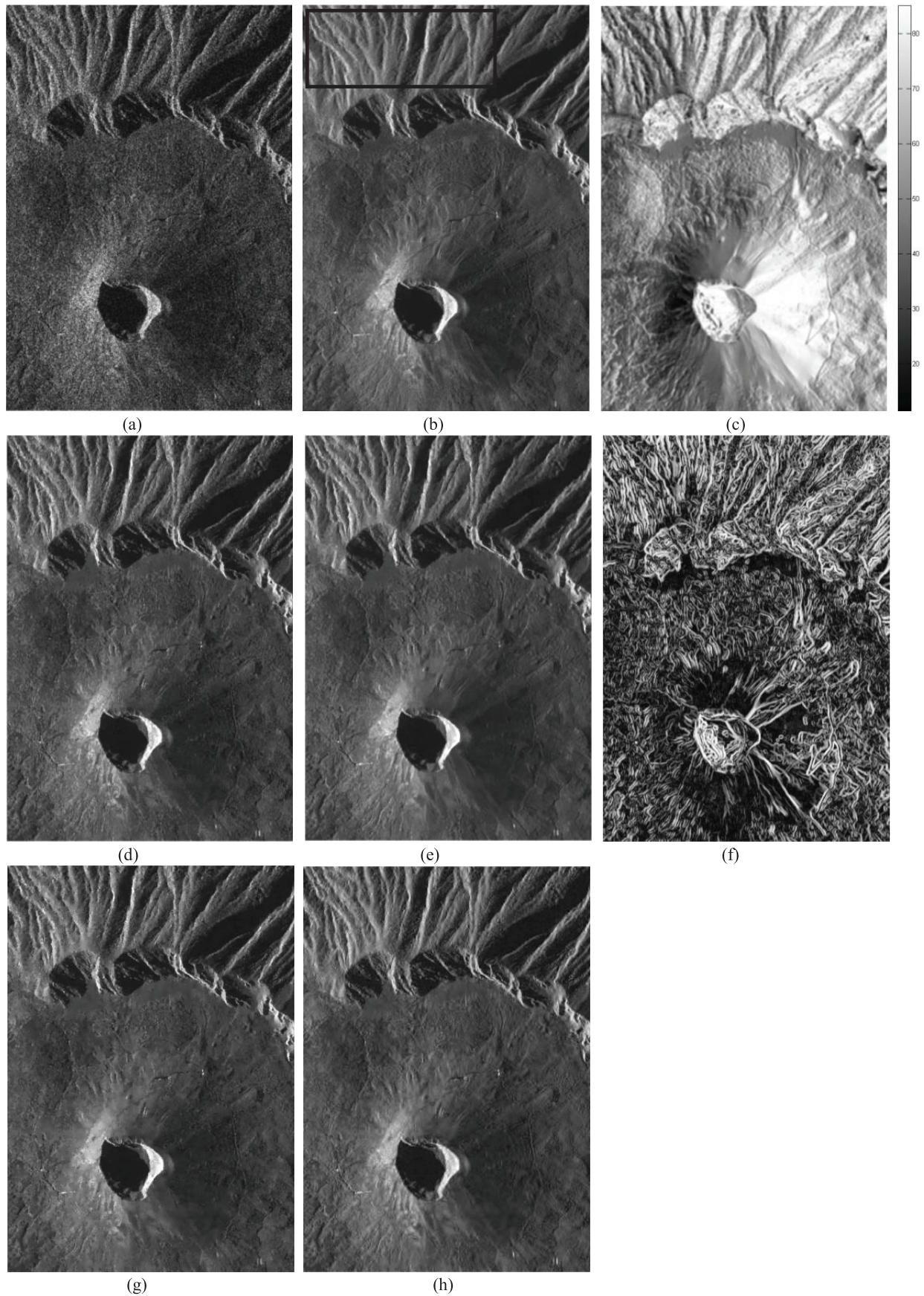


Fig. 6. (a)  $1700 \times 1200$  subset of a COSMO-SkyMed single-look stripmap SAR image of the Vesuvius volcano close to Naples, Italy. (b) Reference image obtained via a temporal multilook of 42 SAR images. The black box indicates the area selected for coefficient of variation computation. (c) Local incidence angle in azimuth-slant range derived from a DEM obtained with a Lidar system. (d) SARBM3D. (e) SB-SARBM3D. (f) Weight map in the range 0–1. (g) NL-SAR. (h) MAP-S.

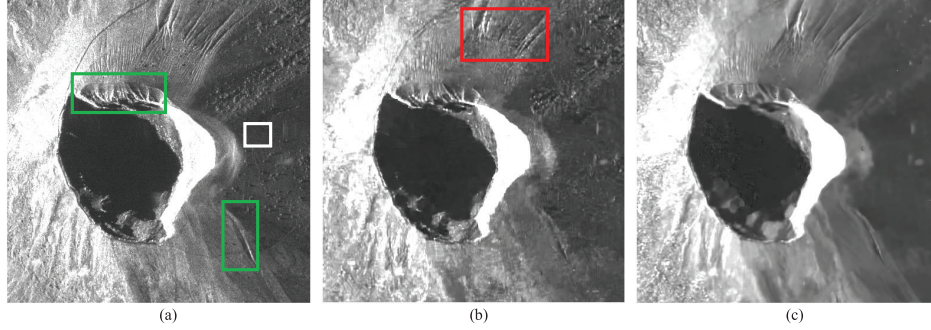


Fig. 7. Zoom of the crater. (a) Reference. (b) SARBM3D. (c) SB-SARBM3D. Green boxes indicate some features better preserved thanks to the *a priori* scattering information; red box indicates some artifacts removed or attenuated w.r.t. SARBM3D. White box indicates the region where the ENL is computed.

[46], and provides reliable information on the image details. In order to reduce false alarms in the presence of topography (i.e., to separate nontopographic edges from those caused by terrain topography), we apply the same detector to the local incidence angle map, obviously without any virtual multilooking, obtaining a further ratio map  $r_\theta$  in the range 0–1. This step allows us to correctly identify nontopographic edges, man-made structures, and homogeneous areas by evaluating the similarity between the two obtained maps  $r_I$  and  $r_\theta$ : similar values reflect gentle topography or homogeneous flat regions; dissimilar values reflect the presence of nontopographic edges and/or man-made structures. Accordingly, the output weight map  $w$  is defined based on the similarity between  $r_I$  and  $r_\theta$

$$w(s) = 1 - \min \left( \frac{r_I(s)}{r_\theta(s)}, \frac{r_\theta(s)}{r_I(s)} \right). \quad (13)$$

#### IV. EXPERIMENTAL RESULTS

Due to the lack of speckle-free SAR images, assessing the performance of despeckling algorithms is a difficult task. Speckle rejection is easily measured through the equivalent number of looks (ENL), computed in homogeneous areas of the image, but detail preservation is typically evaluated only qualitatively through visual inspection. Quantitative measures, however, can be obtained through simulation. To this end, a common approach is to inject speckle on optical images, but these simulated SAR images differ profoundly from the real-world ones, leading to measures that may have little sense. To solve these problems, a benchmarking framework for despeckling was recently proposed in [47], where a physical-based SAR raw signal and image simulator [48] is used to generate realistic SAR images. For some selected canonical scenes, an arbitrary number of single-look realizations can be generated, allowing one to obtain a virtually speckle-free reference by temporal multilooking. We will follow this approach, here, and consider two relevant scenes, computing for each one several objective measures of performance. These simulated scenes enable the numerical comparison between different techniques, providing solid insight into the main advantages and disadvantages of each one. Therefore, we will use them in the next section to analyze the improvements granted over SARBM3D

by the proposed SB version. Then, in the last part of the section, we will analyze performance on real-world SAR images, comparing results with those provided by some state-of-the-art reference techniques, in particular, the NL-SAR [26] and MAP-S [13] filters. In this case, apart from some basic numerical measures, we will rely mostly on visual inspection to assess despeckling quality. To ensure reproducibility of the results, the executable code of the proposed algorithm is available online at <http://www.grip.unina.it>, together with the simulated SAR images and the corresponding DEMs projected in the azimuth-slant range coordinate systems and coregistered with the SAR data.

##### A. Results on Simulated SAR Images

In order to test the proposed algorithm in different scenarios, two suitable scenes are defined, and the corresponding SAR images are generated by means of the SARAS simulator. The first one has a sinusoidal DEM, with constant geometrical and electromagnetic parameters (Fig. 4). A more realistic mixed scene is considered in the second case, having a fractal DEM with constant parameters on the right side, and four square patches with flat DEM and different electromagnetic parameters on the left side (Fig. 5). In particular, for both the sinusoidal and the fractal DEM, we assume  $H = 0.8$ ,  $T = 10^{-4}$  m, relative dielectric constant  $\epsilon_r = 4$ , electrical conductivity  $\sigma_c = 10^{-2}$  S/m. The four flat patches, instead, have electromagnetic parameters (clockwise from top-left):  $\epsilon_r = 10, \sigma_c = 10^{-2}$  S/m;  $\epsilon_r = 4, \sigma_c = 10^{-3}$  S/m;  $\epsilon_r = 4, \sigma_c = 10^{-3}$  S/m;  $\epsilon_r = 80, \sigma_c = 4$  S/m, the second and third patches sharing the same electromagnetic parameters. The parameters of the SARAS simulator are set so as to generate images with the same characteristics as those acquired by the COSMO-SkyMed sensor [49]. All test images have size  $512 \times 512$  pixels, and for each scene, 512 independent single-look realizations are generated. By averaging them, a 512-look image is obtained, which is almost speckle-free and represents therefore a good basis to compute full-reference quality measures. In Figs. 4 and 5, we show, for both scenes, (a) a sample single-look SAR image, (b) the 512-look reference, and (d) the despeckled images output by SARBM3D, and (e) SB-SARBM3D. The latter is based on the prior scattering information evaluated via (8) from (c) the local incidence angle

map, and on (f) the weight map used for combination. It is worth underlining that, although the scattering model is able to take into account also nontopographic inhomogeneities of the sensed surface, such as changes of the dielectric constant or the microscopic roughness, this information is not taken into account here by the SB-SARBM3D filter. In this way, we simulate a more realistic scenario characterized by the lack of prior knowledge on such parameters.

Performance evaluation is carried out by computing some of the objective measures proposed in [47]. In particular, besides the well-known ENL, the mean of intensity (MoI) accounts for possible biases in the output, the variance of ratio (VoR) gives indication on under- and oversmoothing phenomena, and edge smearing (ES) and correlation index ( $C_x$ ) provide information on the preservation of edges and textures, respectively, while the signal-to-noise ratio (SNR) and the mean structure-similarity index (MSSIM) are well-known global measures of distortion. In the presence of a continuously varying SAR image intensity, as in the sinusoidal case, SARBM3D exhibits some clear artifacts [see Fig. 4(d)] that greatly affect the output image quality. The prior information about scattering reduces dramatically these artifacts [see Fig. 4(e)], improving significantly the image quality. In fact, these artifacts are due to random speckle patterns in the input image that are reinforced by nonlocal filtering. Of course, no such patterns exist in the DEM-related SB image. This latter contribute prevails in the first-pass estimate, since the homogeneity of geometrical and electromagnetic parameters, and the absence of man-made structures, gives rise to a weight map [Fig. 4(f)] with values uniformly close to zero. The objective performance indicators reported in Table I confirm these observations. The proposed SB-SARBM3D filter improves significantly w.r.t. the original version in terms of VoR and SNR (about 3 dB), while very close values are observed for  $C_x$ , which makes sense given the absence of texture, and MSSIM, which is little affected by local artifacts.

In the more realistic mixed scene, both topographic and nontopographic related variations in SAR intensity are present. This scene was designed to evaluate the behavior of the algorithm in different situations, such as the homogeneous areas, edges, and topography. As expected, SARBM3D provides a very good edge and texture preservation [see Fig. 5(d)] thanks to the nonlocal approach, while visible artifacts appear, again, in the homogeneous areas, especially in regions close to the edges. In these areas, the DEM-based prior information allows for a much better speckle suppression, increasing the ENL from about 300 for SARBM3D to over 1800 with SB-SARBM3D (see Table II). Because of the assumed lack of information about the variations of electromagnetic parameters, the scattering-based contribute does not “see” the edges in the left side of the image. This might potentially cause a significant ES. However, these edges are well captured by the ratio-edge detector operating on the input SAR image, leading to large values in the weight map of Fig. 5(f). Therefore, the first-pass image coincides largely with the one output by SARBM3D, leading to almost as good an ES value. The SNR figure confirms the overall improvement of the proposed filter w.r.t. SARBM3D, thanks to the *a priori* scattering information.

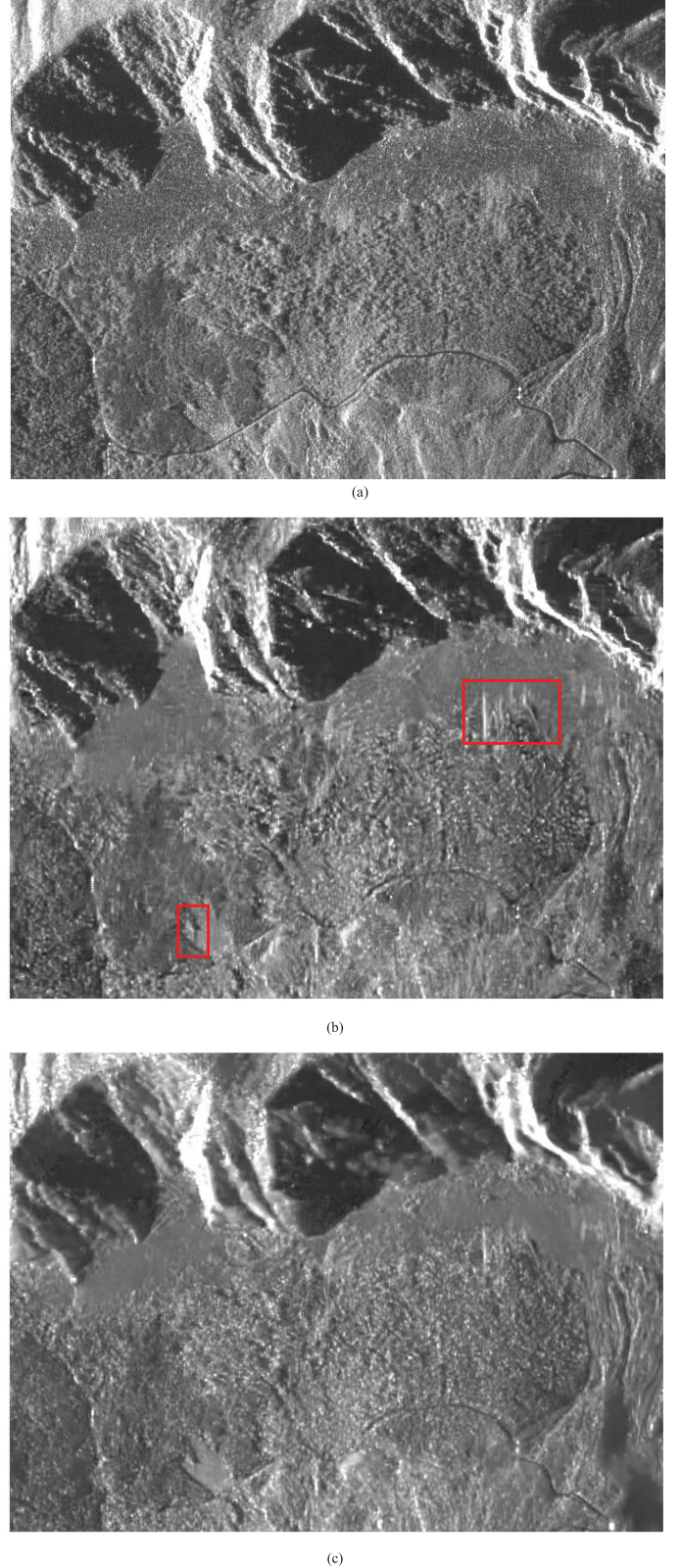


Fig. 8. Zoom of a flat region at the foot of the Mt. Somma. (a) Reference. (b) SARBM3D. (c) SB-SARBM3D. Red boxes indicate some artifacts removed or attenuated.

### B. Results on Actual SAR Images

The proposed algorithm was also applied to two subsets of an actual single-look stripmap COSMO-SkyMed SAR image

TABLE II  
PERFORMANCE PARAMETERS FOR THE MIXED CASE

	Mol	VoR	SNR	$C_x$	ES	MSSIM	ENL
Clean	1.000	1.000	$\infty$	1.898	0.000	1.000	503.78
Noisy	0.997	–	–1.878	2.777	0.025	0.959	0.98
SARBM3D	0.967	0.724	6.916	<b>1.777</b>	<b>0.060</b>	0.995	319.79
SB-SARBM3D	<b>0.972</b>	<b>0.810</b>	<b>8.594</b>	1.723	0.077	<b>0.996</b>	<b>1864.50</b>

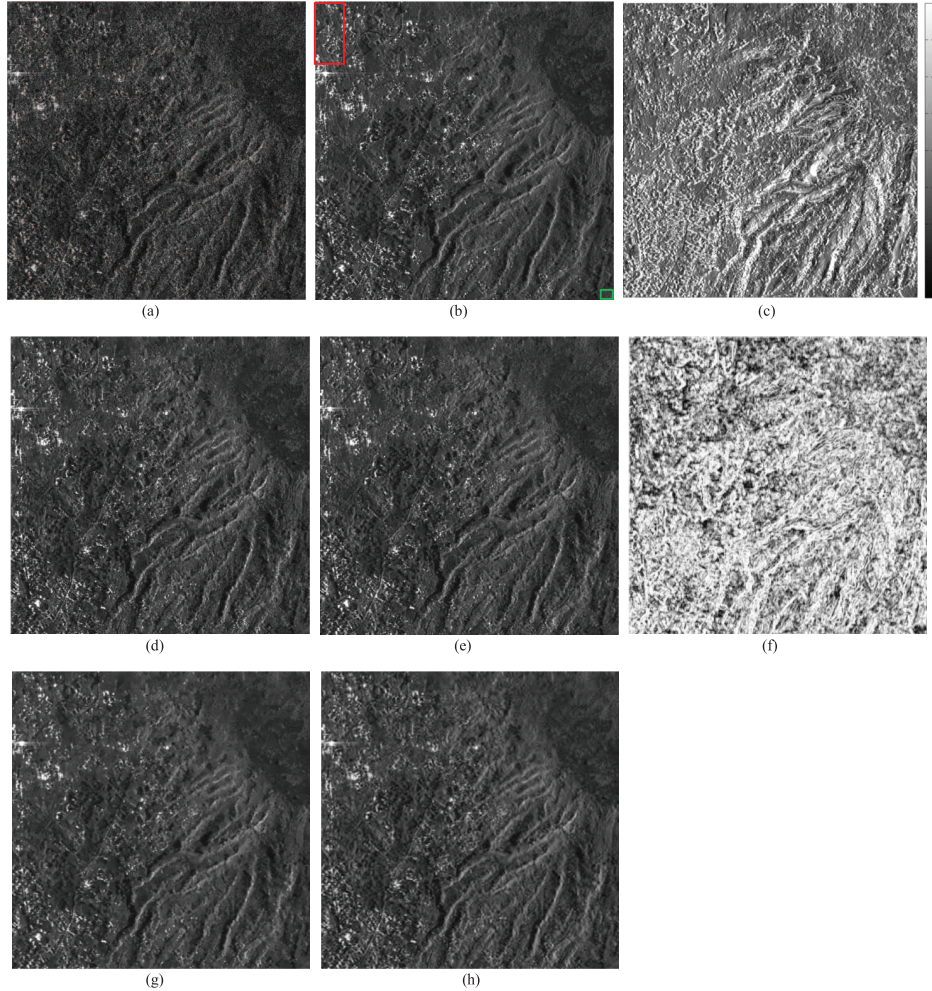


Fig. 9. (a)  $1000 \times 1000$  subset of a COSMO-SkyMed single-look stripmap SAR image of the Vesuvius volcano close to Naples, Italy, and relevant to a partly urbanized area. (b) Image obtained via a temporal multilook of 42 SAR images; ENL = 49.0. (c) Local incidence angle in azimuth-slant range derived from a DEM obtained with a Lidar system. (d) SARBM3D; ENL = 38.1. (e) SB-SARBM3D; ENL = 50.7. (f) Weight map in the range 0–1. (g) NL-SAR; ENL = 62.1. (h) MAP-S; ENL = 62.9. Red marked area is zoomed in Fig. 10, and ENL is evaluated in the green box.

acquired over the Vesuvius-Mt. Somma complex close to Naples, Italy, on August 3, 2011. The first image is  $1700 \times 1200$  pixels and is relevant to a natural area with some sparse man-made objects [Fig. 6(a)]; the second subset is  $1000 \times 1000$  pixels and is relevant to a partly urbanized area at the foot of the Vesuvius mountain [Fig. 9(a)]. The radar look-angle is  $44^\circ$ , while the pixel spacing is 2.07 and 1.17 m in azimuth and slant range, respectively; the operating frequency is 9.6 GHz. For what concerns the natural scenario, we use a 42-look SAR image obtained via temporal multilook as reference [Fig. 6(b)], while the mixed scenario in Fig. 9 deserves a specific comment. Indeed, due to the fast temporal changes characterizing

an urban scenario (mainly due to the presence of vehicles) and the high resolution of the COSMO-SkyMed sensor, some differences between the single-look and the 42-look images are present, as in the red circles in the zoomed region in Fig. 10(a) and (b). Consequently, the 42-look image is not a suitable reference image and no synthetic parameters are evaluated for this scenario, but for the ENL in a homogeneous natural region. Indeed, only a visual inspection is conducted for the quality assessment of the filters.

The local incidence angle maps [Figs. 6(c) and 9(c)] are obtained from a DEM acquired with a Lidar system. Figs. 6(d)–(e) and 9(d)–(e) show the SARBM3D and the

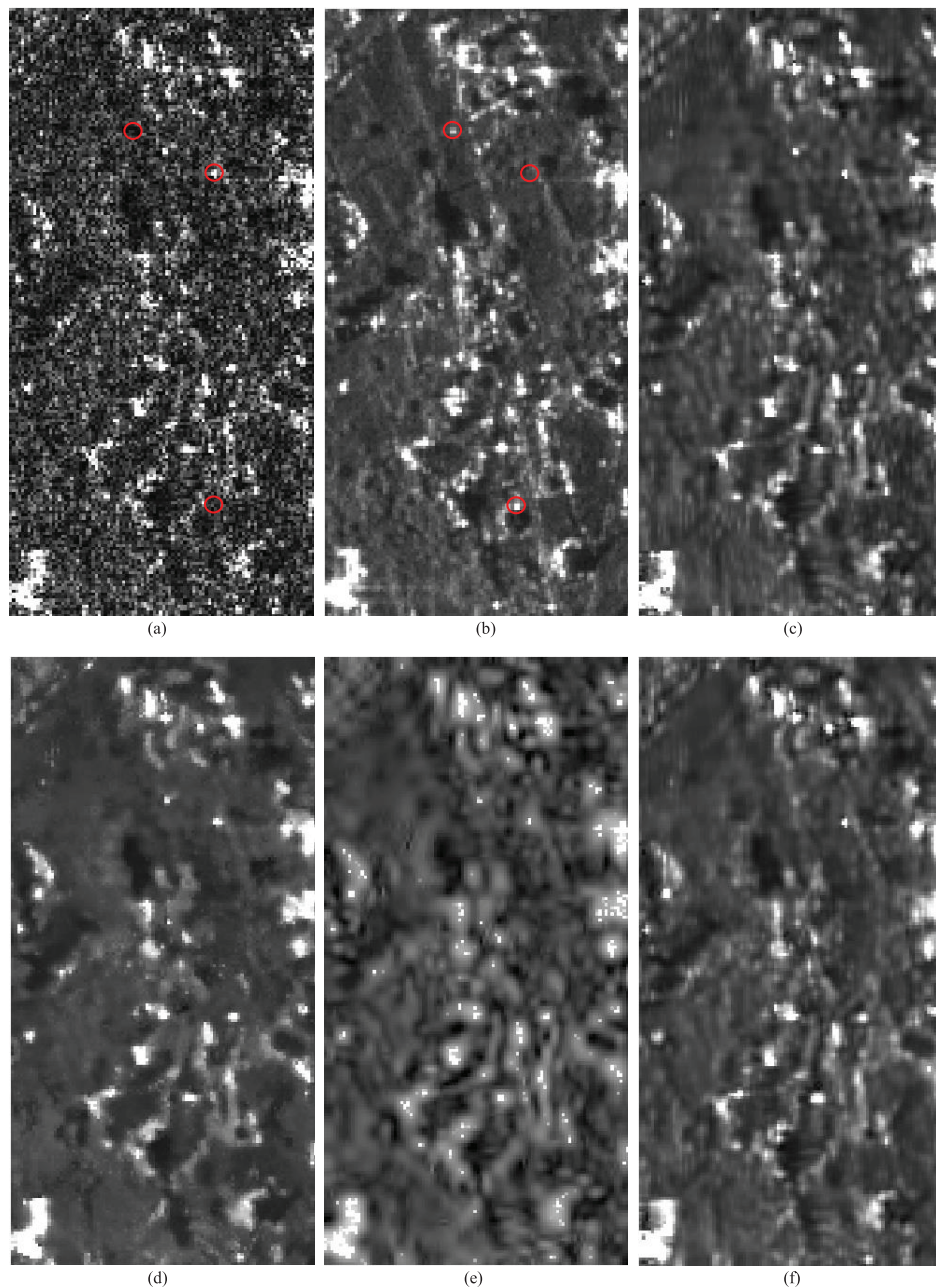


Fig. 10. Zoom of the red marked area in Fig. 9(b). (a) Single-look. (b) 42-look image. (c) SARBM3D. (d) NL-SAR. (e) MAP-S. (f) SB-SARBM3D. Differences between the single and the multilook images are red circled.

proposed filter outputs for the natural and urban scenarios, respectively; Figs. 6(f)–9(f) show the weight maps; in Figs. 6(g) and 9(g), the output of the NL-SAR filter is depicted, while in Figs. 6(h) and 9(h), despeckled images using the MAP-S filter are shown. The Hurst exponent has been evaluated through the algorithm proposed by Di Martino *et al.* in [28]. In order to evaluate the texture preservation capability for the natural scenario, the coefficient of variation is computed on a uniformly textured region of the Mt. Somma [black box in Fig. 6(b)]. For what concerns the natural scenario, despite the absence of nontopographic edges, the image presents some brilliant points to be preserved. As the weight map shows, the proposed ratio detector correctly identifies most of them penalizing the scattering model with a high weight. Due to the strong topography and

geometric distortion (layover and shadowing), the ratio detector provides some false alarms identifying also topographic edges in correspondence of the crater and the Mt. Somma ripples. Despite an overall similarity between the SARBM3D and its SB version outputs, zooms in Figs. 7 and 8 show the better reliability of SB-SARBM3D result especially in terms of removal of the artifacts that affect SARBM3D filter. In particular, the SARBM3D despeckled image presents repetitive horizontal and vertical structures not present in the reference that could significantly affect a correct data interpretation. The *a priori* scattering information allows for a significant reduction of these artifacts. Unfortunately, synthetic parameters are not yet able to reward artifacts removal. A better smoothing is reached by the SB-SARBM3D filter, as witnessed by the

TABLE III  
PERFORMANCE PARAMETERS FOR THE ACTUAL IMAGE OF A NATURAL SCENE

	Mol	VoR	SNR	$C_x$	MSSIM	ENL
Reference	1.000	1.000	$\infty$	1.001	1.000	24.02
Noisy	1.000	—	-0.796	1.734	0.963	0.98
SARBM3D	0.970	0.625	<b>5.447</b>	<b>0.998</b>	0.990	71.15
SB-SARBM3D	0.968	<b>1.014</b>	5.352	0.891	<b>0.991</b>	<b>92.65</b>
NL-SAR	0.965	1.094	4.565	0.878	<b>0.991</b>	74.49
MAP-S	<b>0.988</b>	14.040	3.729	0.975	0.989	52.80

VoR parameter in Table III. A good speckle reduction together with satisfactory texture preservation is provided by NL-SAR and MAP-S filters. However, the MAP-S algorithm produces some visible artifacts and deformation of the SAR data, such as some brilliant points in correspondence of high intensity data. The VoR indicator for the MAP-S suggests some malfunctioning of the filter in specific scenarios, as shown in the literature [47]. Finally, the SB-SARBM3D filter presents better speckle reduction in homogeneous areas as shown by the higher ENL computed in the white box of Fig. 7(a).

The mixed scenario shown in Fig. 9 shows the behavior of the proposed SB-SARBM3D in a partly man-made scenario in which, together with the single-bounce diffusion, other scattering phenomena—not taken into account within the proposed scattering model—occur, such as multiple-bounce scattering. Reasonably, in such a scenario, the filter assigns a major weight to SARBM3D, but for the natural area in the right-up corner, as the weight map in Fig. 9(f) shows. Consequently, SB-SARBM3D inherits most of the detail-preservation capability of SARBM3D in the urban area [see Fig. 10(f)], in which the proposed scattering model is not adequate, and provides a better speckle reduction w.r.t. the SARBM3D filter in homogeneous areas, as the ENL shows (Fig. 9). The best ENL value is provided by the MAP-S filter. However, it must be noted that the MAP-S filter, although it is capable of retaining most of the man-made structures, causes visible distortions of the SAR data. In this scenario, good performance is provided also by the NL-SAR filter, whose capability to preserve the urban features and drastically remove speckle without inserting visible artifacts can be visually and quantitatively assessed.

A last remark about computational complexity is in order. Due to the additional steps of weights evaluation, DEM projection, and Hurst coefficient evaluation, the proposed SB-SARBM3D presents a computational load larger than the original SARBM3D filter. In particular, for all the experiments run, the proposed SB-SARBM3D requires about four times the computational time of SARBM3D. The increase of computational time is mainly due to the weight evaluation phase.

## V. CONCLUSION

In this paper, we have proposed a SB modified version of the SARBM3D filter originally proposed in [24]. The new version improves the first-step estimate of SARBM3D by taking into account prior information about electromagnetic scattering of the sensed surface. To this aim, the surface roughness

of natural surfaces has been modeled as a 2-D fBm stochastic process, while scattering phenomena have been modeled via an SPM formulation suitable for fractal surfaces. Despite the numerous parameters influencing surface scattering, only the local incidence angle is assumed to be known, which in turn requires a DEM of the underlying surface. Estimates provided by the first step of SARBM3D and by the assumed scattering model present complementary properties. In fact, SARBM3D provides good edge and detail preservation, while introducing visible artifacts in homogeneous and flat regions. Conversely, the scattering model with the assumed prior knowledge describes quite well the response of electromagnetically homogeneous natural areas, while it is inaccurate in describing scattering from nontopographic edges and man-made structures, unless additional information is available. Consequently, the new first step estimation is obtained by combining the prior scattering information and the first-step SARBM3D estimate with adaptive weights, related to the local reliability of the two terms. In particular, the weight map is computed using the ratio edge and line detectors developed in [45]. The filter weight evaluation is designed to assign a major weight to the *a priori* scattering information in regions with topographic-related SAR intensity variations and, conversely, to assign a major weight to SARBM3D in regions with nontopographic-related SAR intensity variations. The new SB-SARBM3D filter has been applied to both simulated and real SAR images and compared with the original SARBM3D and other state-of-the-art references. The proposed filter exhibits promising results especially in homogeneous flat and gently sloped areas, providing a better speckle suppression than the state of the art with the same good preservation of details. However, SB despeckling is a novel idea and there is much room for further investigations and analyses in terms of both theoretical studies and experimental results. A major issue for further research is the ability to take into account peculiar scattering mechanisms from both natural and urban areas. At the same time, the research in this field would benefit from better tools for the numerical assessment of performance, including, for example, a quantitative measure of despeckling artifacts.

## REFERENCES

- [1] F. Argenti, A. Lapini, T. Bianchi, and L. Alparone, "A tutorial on speckle reduction in synthetic aperture radar images," *IEEE Geosci. Remote Sens. Mag.*, vol. 1, no. 3, pp. 6–35, Sep. 2013.
- [2] J. S. Lee, "Digital image enhancement and noise filtering by use of local statistics," *IEEE Trans. Pattern Anal. Mach. Intell.*, vol. PAMI-2, no. 2, pp. 165–168, Mar. 1980.

- [3] V. S. Frost, J. A. Stiles, K. S. Shanmugan, and J. C. Holtzman, "A model for radar images and its application to adaptive digital filtering of multiplicative noise," *IEEE Trans. Pattern Anal. Mach. Intell.*, vol. PAMI-4, no. 2, pp. 157–166, Mar. 1982.
- [4] D. T. Kuan, A. A. Sawchuk, T. C. Strand, and P. Chavel, "Adaptive noise smoothing filter for images with signal-dependent noise," *IEEE Trans. Pattern Anal. Mach. Intell.*, vol. PAMI-7, no. 2, pp. 165–177, Mar. 1985.
- [5] A. Lopes, R. Touzi, and E. Nezry, "Adaptive speckle filters and scene heterogeneity," *IEEE Trans. Geosci. Remote Sens.*, vol. 28, no. 6, pp. 992–1000, Nov. 1990.
- [6] E. Nezry, A. Lopes, and R. Touzi, "Detection of structural and textural features for SAR images filtering," in *Proc. IEEE Int. Geosci. Remote Sens. Symp. (IGARSS'91)*, 1992, pp. 2169–2172.
- [7] R. Touzi, A. Lopes, and P. Bousquet, "A statistical and geometrical edge detector for SAR images," *IEEE Trans. Geosci. Remote Sens.*, vol. 26, no. 6, pp. 764–773, Nov. 1988.
- [8] M. Hebar, D. Gleich, and Z. Cucej, "Autobinomial model for SAR image despeckling and information extraction," *IEEE Trans. Geosci. Remote Sens.*, vol. 47, no. 8, pp. 2818–2835, May 2009.
- [9] M. Walessa and M. Datcu, "Model-based despeckling and information extraction from SAR images," *IEEE Trans. Geosci. Remote Sens.*, vol. 38, no. 5, pp. 2258–2269, Sep. 2000.
- [10] F. Argenti and L. Alparone, "Speckle removal from SAR images in the undecimated wavelet domain," *IEEE Trans. Geosci. Remote Sens.*, vol. 40, no. 11, pp. 2363–2374, Nov. 2002.
- [11] J. J. Ranjani and S. J. Thiruvengadam, "Dual-Tree complex wavelet transform based SAR despeckling using interscale dependence," *IEEE Trans. Geosci. Remote Sens.*, vol. 48, no. 6, pp. 2723–2731, Jun. 2010.
- [12] S. Foucher, G. Bénéic, and J. Boucher, "Multiscale MAP filtering of SAR images," *IEEE Trans. Image Process.*, vol. 10, no. 1, pp. 49–60, Jan. 2001.
- [13] T. Bianchi, F. Argenti, and L. Alparone, "Segmentation-based MAP despeckling of SAR images in the undecimated wavelet domain," *IEEE Trans. Geosci. Remote Sens.*, vol. 46, no. 9, pp. 2728–2742, Sep. 2008.
- [14] W. Zhang, F. Liu, L. Jiao, B. Hou, S. Wang, and R. Shang, "SAR image despeckling using edge detection and feature clustering in bandelet domain," *IEEE Geosci. Remote Sens. Lett.*, vol. 7, no. 1, pp. 131–135, Jan. 2010.
- [15] Y. Li, H. Gong, D. Feng, and Y. Zhang, "An adaptive method of speckle reduction and feature enhancement for SAR images based on curvelet transform and particle swarm optimization," *IEEE Trans. Geosci. Remote Sens.*, vol. 49, no. 8, pp. 3105–3116, Aug. 2011.
- [16] S. Foucher, "SAR image filtering via learned dictionaries and sparse representations," in *Proc. IEEE Int. Geosci. Remote Sens. Symp. (IGARSS'08)*, 2008, pp. 229–232.
- [17] Y. Huang, L. Moisan, M. K. Ng, and T. Zeng, "Multiplicative noise removal via a learned dictionary," *IEEE Trans. Image Process.*, vol. 21, no. 11, pp. 4534–4543, Nov. 2012.
- [18] B. Xu, Y. Cui, Z. Li, and J. Yang, "An iterative SAR image filtering method using nonlocal sparse model," *IEEE Geosci. Remote Sens. Lett.*, vol. 12, no. 8, pp. 1635–1639, Aug. 2015.
- [19] A. Buades, B. Coll, and J. M. Morel, "A review of image denoising algorithms, with a new one," *Multiscale Model. Simul.*, vol. 4, no. 2, pp. 490–530, 2005.
- [20] C.-A. Deledalle, L. Denis, G. Poggi, F. Tupin, and L. Verdoliva, "Exploiting patch similarity for SAR image processing: The nonlocal paradigm," *IEEE Signal Process. Mag.*, vol. 31, no. 4, pp. 69–78, Jul. 2014.
- [21] J.-S. Lee, "Digital image smoothing and the sigma filter," *Comput. Vis. Graph. Image Process.*, vol. 24, no. 2, pp. 255–269, 1983.
- [22] J.-S. Lee, J.-H. Wen, T. L. Ainsworth, K.-S. Chen, and A. J. Chen, "Improved sigma filter for speckle filtering of SAR imagery," *IEEE Trans. Geosci. Remote Sens.*, vol. 47, no. 1, pp. 202–213, Jan. 2009.
- [23] C.-A. Deledalle, L. Denis, and F. Tupin, "Iterative weighted maximum likelihood denoising with probabilistic patch-based weights," *IEEE Trans. Image Process.*, vol. 18, no. 12, pp. 2661–2672, Dec. 2009.
- [24] S. Parrilli, M. Poderico, C. V. Angelino, and L. Verdoliva, "A nonlocal SAR image denoising algorithm based on LLMMSE wavelet shrinkage," *IEEE Trans. Geosci. Remote Sens.*, vol. 50, no. 2, pp. 606–616, Feb. 2012.
- [25] D. Cozzolino, S. Parrilli, G. Scarpa, G. Poggi, and L. Verdoliva, "Fast adaptive nonlocal SAR despeckling," *IEEE Geosci. Remote Sens. Lett.*, vol. 11, no. 2, pp. 524–528, Feb. 2014.
- [26] C.-A. Deledalle, L. Denis, F. Tupin, A. Reigber, and M. Jager, "NL-SAR: A unified nonlocal framework for resolution-preserving (Pol) (In) SAR denoising," *IEEE Trans. Geosci. Remote Sens.*, vol. 53, no. 4, pp. 2021–2038, Apr. 2015.
- [27] R. Touzi, "A review of speckle filtering in the context of estimation theory," *IEEE Trans. Geosci. Remote Sens.*, vol. 40, no. 11, pp. 2392–2404, Nov. 2002.
- [28] G. Di Martino, D. Riccio, and I. Zinno, "SAR imaging of fractal surfaces," *IEEE Trans. Geosci. Remote Sens.*, vol. 50, no. 2, pp. 630–644, Feb. 2012.
- [29] G. Franceschetti and R. Lanari, *Synthetic Aperture Radar (SAR) Processing*. Boca Raton, FL, USA: CRC Press, 1999.
- [30] J.-S. Lee, M. Grunes, D. Schuler, E. Pottier, and L. Ferro-Famil, "Scattering-model-based speckle filtering of polarimetric SAR data," *IEEE Trans. Geosci. Remote Sens.*, vol. 44, no. 1, pp. 176–187, Jan. 2006.
- [31] G. Di Martino, A. Di Simone, A. Iodice, D. Riccio, and G. Ruello, "Non-local means SAR despeckling based on scattering," in *Proc. IEEE Int. Geosci. Remote Sens. Symp. (IGARSS'15)*, Milan, Italy, Jul. 2015, pp. 3172–3174.
- [32] G. Di Martino, A. Di Simone, A. Iodice, and D. Riccio, "Scattering-based non-local means SAR despeckling," *IEEE Trans. Geosci. Remote Sens.*, Feb. 2016, doi: 10.1109/TGRS.2016.2520309.
- [33] K. Dabov, A. Foi, V. Katkovnik, and K. Egiazarian, "Image denoising by sparse 3-D Transform-domain collaborative filtering," *IEEE Trans. Image Process.*, vol. 16, no. 8, pp. 2080–2095, Aug. 2007.
- [34] C.-A. Deledalle, L. Denis, and F. Tupin, "How to compare noisy patches? Patch similarity beyond Gaussian noise," *Int. J. Comput. Vis.*, vol. 99, pp. 86–102, 2012.
- [35] O. D'Hondt, S. Guillaso, and O. Hellwich, "Iterative bilateral filtering of polarimetric SAR data," *IEEE J. Sel. Topics Appl. Earth Observ. Remote Sens.*, vol. 6, no. 3, pp. 1628–1639, Jun. 2013.
- [36] L. Torres, S. J. S. Sant'Anna, C. da Costa Freitas, and A. C. Frery, "Speckle reduction in polarimetric SAR imagery with stochastic distances and nonlocal means," *Pattern Recog.*, vol. 47, no. 1, pp. 141–157, 2014.
- [37] L. Verdoliva, R. Gaetano, G. Ruello, and G. Poggi, "Optical-driven non-local SAR despeckling," *IEEE Geosci. Remote Sens. Lett.*, vol. 12, no. 2, pp. 314–318, Feb. 2015.
- [38] K. Falconer, *Fractal Geometry*. Hoboken, NJ, USA: Wiley, 1990.
- [39] J. S. Feder, *Fractals*. New York, NY, USA: Plenum, 1988.
- [40] G. Franceschetti and D. Riccio, *Scattering, Natural Surfaces and Fractals*. New York, NY, USA: Academic, 2007.
- [41] B. Mandelbrot, *The Fractal Geometry of Nature*. San Francisco, CA, USA: Freeman, 1983.
- [42] G. Di Martino, A. Di Simone, A. Iodice, D. Riccio, and G. Ruello, "On shape from shading and SAR images: An overview and a new perspective," in *Proc. IEEE Int. Geosci. Remote Sens. Symp.*, 2014, pp. 1333–1336.
- [43] G. Franceschetti, A. Iodice, S. Maddaluno, and D. Riccio, "A fractal-based theoretical framework for retrieval of surface parameters from electromagnetic backscattering data," *IEEE Trans. Geosci. Remote Sens.*, vol. 38, no. 2, pp. 641–650, Mar. 2000.
- [44] A. Iodice, A. Natale, and D. Riccio, "Retrieval of soil surface parameters via a polarimetric two-scale model," *IEEE Trans. Geosci. Remote Sens.*, vol. 49, no. 7, pp. 2531–2547, Jul. 2011.
- [45] A. Lopes, E. Nezry, R. Touzi, and H. Laur, "Structure detection and statistical adaptive speckle filtering in SAR images," *Int. J. Remote Sens.*, vol. 14, no. 9, pp. 1735–1758, 1993.
- [46] D. Gagnaniello, G. Poggi, G. Scarpa, and L. Verdoliva, "SAR despeckling based on soft classification," in *Proc. IEEE Int. Geosci. Remote Sens. Symp.*, Milan, Italy, Jul. 2015, pp. 2378–2381.
- [47] G. Di Martino, M. Poderico, G. Poggi, D. Riccio, and L. Verdoliva, "Benchmarking framework for SAR despeckling," *IEEE Trans. Geosci. Remote Sens.*, vol. 52, no. 3, pp. 1596–1615, Mar. 2014.
- [48] G. Franceschetti, M. Migliaccio, D. Riccio, and G. Schirinzì, "SARAS: A SAR raw signal simulator," *IEEE Trans. Geosci. Remote Sens.*, vol. 30, no. 1, pp. 110–123, Jan. 1992.
- [49] Italian Space Agency (ASI). (2007). *COSMO-SkyMed System Description & User Guide* [Online]. Available: <http://www.cosmoskymed.it/docs/ASI-CSM-ENG-RS-093-A-CSKSysDescriptionAndUserGuide.pdf>



**Gerardo Di Martino** (S'06–M'09) was born in Naples, Italy, on June 22, 1979. He received the Laurea degree (*cum laude*) in telecommunication engineering and the Ph.D. degree in electronic and telecommunication engineering from the University of Naples Federico II, Naples, Italy, in 2005 and 2009, respectively.

From 2009 to 2010, he conducted a research on indoor electromagnetic propagation and localization of unknown transmitters with the Department of Biomedical, Electronic, and Telecommunication Engineering, University of Naples Federico II, through grants from the same university. From 2010 to 2012, he worked on a project financed by the Italian Space Agency aimed at the development of techniques for information extraction from high-resolution SAR images of urban and natural areas. From 2012 to 2014, he was a Research Fellow with the Department of Electrical Engineering and Information Technology, University of Naples Federico II, working on a project regarding maritime surveillance with SAR data. From 2014 to 2015, he conducted a research in the field of electromagnetic propagation in harbor scenarios and innovative network architectures through grants received from the Italian National Consortium for Telecommunications. He is currently a Research Fellow with the Department of Electrical Engineering and Information Technology, University of Naples Federico II, working on a project regarding sparse antenna arrays. His research interests include microwave remote sensing and electromagnetics, with particular focus on modeling of the electromagnetic scattering from natural surfaces and urban areas, SAR signal processing and simulation, information retrieval from SAR data, and remote-sensing techniques for developing countries.



**Alessio Di Simone** was born in Torre del Greco, Naples, Italy, on September 11, 1989. He received the B.Sc. and M.Sc. Laurea degrees (*cum laude*) in telecommunication engineering from the University of Naples Federico II, Naples, Italy, in 2011 and 2013, respectively. He is currently pursuing the Ph.D. degree in information technology and electrical engineering at the University of Naples Federico II.

His research interests include the field of microwave remote sensing and electromagnetics: modeling of the electromagnetic scattering from natural surfaces, SAR data simulation, information retrieval, and despeckling.

Mr. Di Simone was awarded a prize for the Best Master Thesis in Remote Sensing by the IEEE SOUTH ITALY GEOSCIENCE AND REMOTE SENSING Chapter in 2015.



**Antonio Iodice** (S'97–M'00–SM'04) was born in Naples, Italy, in 1968. He received the Laurea degree (*cum laude*) in electronic engineering and the Ph.D. degree in electronic engineering and computer science from the University of Naples Federico II, Naples, Italy, in 1993 and 1999, respectively.

In 1995, he was with the Research Institute for Electromagnetism and Electronic Components, Italian National Council of Research (IRECE-CNR), Naples, Italy, and from 1999 to 2000 with Telespazio S.p.A., Rome, Italy. From 2000 to 2004, he was a Research Scientist with the Department of Electronic and Telecommunication Engineering, University of Naples Federico II. He is currently a Professor of Electromagnetics with the Department of Electrical Engineering and Information Technology, University of Naples Federico II. He has authored or co-authored more than 300 papers, of which more than 70 published on refereed journals, and the others on proceedings of international and national conferences. His research interests include microwave remote sensing and electromagnetics: modeling of electromagnetic scattering from natural surfaces and urban areas, simulation and processing of synthetic aperture radar (SAR) signals, and electromagnetic propagation in urban areas.

Prof. Iodice has been involved as a Principal Investigator or Coinvestigator in several projects funded by European Union (EU), Italian Space Agency (ASI), Italian Ministry of Education and Research (MIUR), Campania Regional Government, and Private Companies. He is the Chair of the IEEE SOUTH ITALY GEOSCIENCE AND REMOTE SENSING Chapter. He was the recipient of the 2009 "Sergei A. Schelkunoff Transactions Prize Paper Award" from the IEEE Antennas and Propagation Society for the Best Paper published in 2008 on the IEEE TRANSACTIONS ON ANTENNAS AND PROPAGATION.



**Giovanni Poggi** (M'14) received the Laurea degree in electronic engineering from the University of Naples Federico II, Naples, Italy, in 1988.

He is currently a Professor of Telecommunications with the University of Naples Federico II, and Coordinator of the Telecommunication Engineering School. His research interests include statistical image processing such as compression, restoration, segmentation, and classification, with application to the area of remote sensing, both optical and SAR, and digital forensics.

Prof. Poggi has been an Associate Editor for the IEEE TRANSACTIONS ON IMAGE PROCESSING and *Elsevier Signal Processing*.



**Daniele Riccio** (M'91–SM'99–F'14) was born in Naples, Italy. He received the Laurea degree (*cum laude*) in electronic engineering from the University of Naples Federico II, Naples, Italy, in 1989.

His career has been developed with the University of Naples Federico II. He is currently a Full Professor of electromagnetic theory and remote sensing with the Department of Electrical Engineering and Information Technology, University of Naples Federico II. He is the Head of the Ph.D. School in Information Technology and Electrical Engineering with the University of Napoli Federico II. As additional activities, he was a Research Scientist with the Italian National Research Council at the Institute for Research on Electromagnetics and Electronic Components (1989–1994), a Guest Scientist with the German Aerospace Centre (DLR), Munich, Germany (1994 and 1995), and a Lecturer to the Ph.D. programme with the Universitat Politècnica de Catalunya, Barcelona, Spain (2006) and with the Czech Technical University, Prague, Czech Republic (2012). He has authored three books, including *Scattering, Natural Surfaces, and Fractals* (2007), and more than 350 papers. His research interests include microwave remote sensing, electromagnetic scattering, synthetic aperture radar with emphasis on sensor design, data simulation and information retrieval, as well as application of fractal geometry to remote sensing.

Prof. Riccio is currently a Member of the Cassini Radar Science Team, Principal Investigator for international research projects on exploitation of remote sensing data and design of synthetic aperture radars, and participates to technical committees of international symposia on electromagnetics and remote sensing. He serves as an Associate Editor for some journals on Remote Sensing. He was the recipient of the 2009 Sergei A. Schelkunoff Transactions Prize Paper Award for the best paper published in 2008 on the IEEE TRANSACTIONS ON ANTENNAS AND PROPAGATION.



**Luisa Verdoliva** (M'13) received the Laurea degree in telecommunications engineering and the Ph.D. degree in information engineering from the University of Naples Federico II, Naples, Italy, in 1998 and 2002, respectively.

She is currently an Assistant Professor with the University Federico II of Naples. Her research interests include image processing, in particular compression and restoration of remote-sensing images, both optical and SAR, and digital forensics.

Dr. Verdoliva is a Member of the IEEE Information Forensics and Security Technical Committee (2016–2018).